



OPEN ACCESS

EDITED BY

Zhiwei Guo,
Tongji University, China

REVIEWED BY

Biao Yang,
National University of Defense
Technology, China
Xiao-Dong Chen,
Sun Yat-sen University, China

*CORRESPONDENCE

Bo Hou,
✉ houbo@suda.edu.cn

SPECIALTY SECTION

This article was submitted
to Optics and Photonics,
a section of the journal
Frontiers in Physics

RECEIVED 11 November 2022

ACCEPTED 15 December 2022

PUBLISHED 06 January 2023

CITATION

Pan X, Li H, Dong W, Zhou X, Xing K-A,
Hu C, Wang G and Hou B (2023), Nodal
degeneracy of guided modes in uniaxial
crystal slabs.
Front. Phys. 10:1095669.
doi: 10.3389/fphy.2022.1095669

COPYRIGHT

© 2023 Pan, Li, Dong, Zhou, Xing, Hu,
Wang and Hou. This is an open-access
article distributed under the terms of the
[Creative Commons Attribution License
\(CC BY\)](https://creativecommons.org/licenses/by/4.0/). The use, distribution or
reproduction in other forums is
permitted, provided the original
author(s) and the copyright owner(s) are
credited and that the original
publication in this journal is cited, in
accordance with accepted academic
practice. No use, distribution or
reproduction is permitted which does
not comply with these terms.

Nodal degeneracy of guided modes in uniaxial crystal slabs

Xinyang Pan¹, Haitao Li¹, Weijie Dong¹, Xiaoxi Zhou¹,
Ke-Ao Xing², Chuandeng Hu³, Gang Wang¹ and Bo Hou^{1,4*}

¹School of Physical Science and Technology and Collaborative Innovation Center of Suzhou Nano Science and Technology, Soochow University, Suzhou, China, ²Department of Integrated Technology and Control Engineering, School of Aeronautics, Northwestern Polytechnical University, China, ³Shenzhen Fantwave Tech Co., Ltd, Shenzhen, China, ⁴Key Laboratory of Modern Optical Technologies of Ministry of Education and Key Lab of Advanced Optical Manufacturing Technologies of Jiangsu Province, Suzhou, China

We study the dispersions of the guided modes in the continuous uniaxial crystal slab waveguide and engineer their degeneracies through dielectric anisotropy. By switching the uniaxial positivity and negativity, we can obtain distinctive nodal types, point and line, for the lowest degeneracy in frequency. The mirror symmetry protections, M_x and M_y , are pointed out, and the degeneracy properties are intuitively analyzed through comparing the approximate slopes of the guided modes. Our results reveal a link between the lowest nodal types and the positivity/negativity of the uniaxial crystal, and provide a new approach to regulate the topology of degeneracy in two-dimensional photonic bands.

KEYWORDS

nodal line, nodal points, uniaxial crystal, topological transformation, band degeneracy, symmetry, guided mode

Introduction

Recently, a research focus is concentrated on nodal degeneracy in band diagrams in periodical structures [1–5], such as quantum materials, photonic crystals, and phononic crystals, because new physics and novel applications are anticipated arising from peculiar band degeneracies including point degeneracy [6–16], line/loop degeneracy [17–28], nodal chain degeneracy [29–31], nodal surface degeneracy [32, 33] and so on.

Band degeneracy is generally enforced by symmetry in the physical system. It is well known that photonic guided waves in confined structures can be classified into transverse electric (TE) and transverse magnetic (TM) modes in terms of mirror symmetry [our meanings of “TE” and “TM” adapted to classical waveguide theory, see [34]]. Taking an example of an isotropic dielectric slab waveguide, both modes evolve out from the light cone in free space, and their dispersion curves are rapidly asymptotic to the light cone in dielectrics as propagation constant increasing. Because of the asymptotic parallelism, the TE and TM dispersions cross rarely to form the degeneracy beyond the free space light cone, which is schematically depicted in Figure 1B. On the other hand, the slopes of the TE and TM modes in the dispersion diagram can be tailored in a polarization-distinguishable way through introducing the uniaxial anisotropy to the dielectric slab. The tailoring

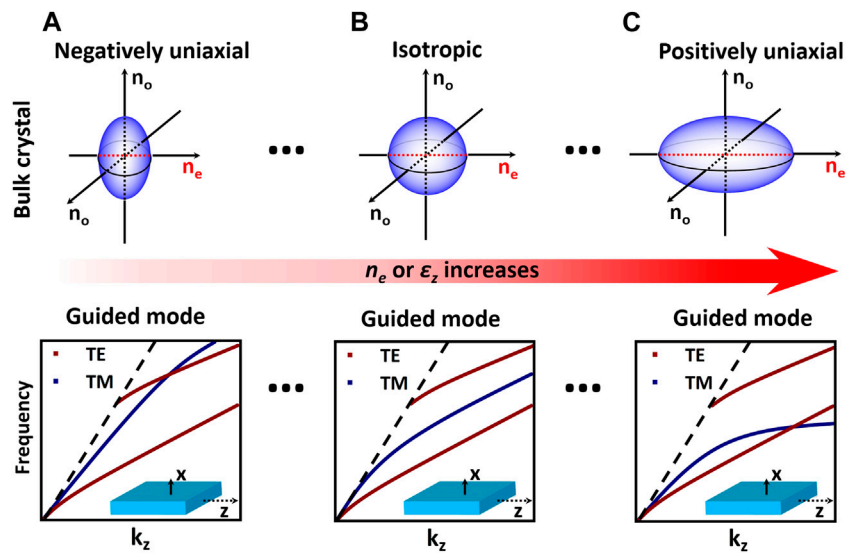


FIGURE 1 Schematics for the index ellipsoids (upper row) in a uniaxial bulk crystal where the optical axis n_e is along the horizontal direction, and the guided modes (lower row) in the uniaxial crystal slab with the finite thickness along the x -direction as illustrated by the insets. The propagation of the guided modes is assumed along the optical axis, i.e., horizontal direction, labeled as z -axis in the insets. The dark red lines denote TE modes, the dark blue lines denote TM modes, and the dash lines denote the light line. n_e or ϵ_z increases from left to right, as indicated by the arrow, and shows (A) negatively uniaxial, (B) isotropic, and (C) positively uniaxial cases.

mechanism is rooted on the refractive index difference which is manifested likewise in the propagation of ordinary and extraordinary light in a uniaxial bulk crystal [35], seeing the index ellipsoid in Figure 1.

In the study, we start with an isotropic dielectric slab, where TE and TM modes are not degenerate. By changing the dielectric constant into the uniaxial permittivity tensor and tuning the component of the tensor along the propagation direction, we show the slope of TM modes can either increase or decrease significantly while maintaining the slope of TE modes, which corresponds to the positively and negatively uniaxial anisotropy, respectively. Thus, the crossing between TE and TM modes can be engineered, as illustrated in Figure 1. Furthermore, the mirror symmetry along the out-of-slab direction imposes an extra enforcement on the degeneracy and leads to distinctive nodal types, Dirac point (DP) and Dirac line (DL), in the positive and negative uniaxial cases for the lowest degeneracy in frequency.

Guided mode in uniaxial crystal slabs

Here, we consider a two-dimensional (2D) infinite (along y - and z -directions), uniaxial crystal slab (finite thickness $d = 2$ mm in the x -direction) with non-magnetic permeability ($\mu/\mu_0 = 1$; μ_0 being the permeability in vacuum). The slab is located in free space where the wave is assumed propagating along the z -direction, and the permittivity tensor has the diagonal form

$diag[n_o^2, n_o^2, n_e^2] \cdot \epsilon_0$ with n_o (n_e) being the refractive index of ordinary (extra-ordinary) light and ϵ_0 being the permittivity in vacuum. The dielectric principal axis in the uniaxial crystal is spanned by (n_o, n_o, n_e) , shown in Figure 2A, where θ denotes the in-plane rotation of the optical axis. When $\theta = 0$, the anisotropic permittivity tensor ϵ_i of the slab can be expressed in the (x, y, z) coordinate system as:

$$\bar{\epsilon}_i/\epsilon_0 = \begin{bmatrix} \epsilon_x/\epsilon_0 & 0 & 0 \\ 0 & \epsilon_y/\epsilon_0 & 0 \\ 0 & 0 & \epsilon_z/\epsilon_0 \end{bmatrix} = \begin{bmatrix} n_o^2 & 0 & 0 \\ 0 & n_o^2 & 0 \\ 0 & 0 & n_e^2 \end{bmatrix} \quad (1)$$

where ϵ_i is the permittivity along the i ($i = x / y / z$) direction with relative value $\epsilon_{xr} = \epsilon_x/\epsilon_0 = n_o^2$, $\epsilon_{yr} = \epsilon_y/\epsilon_0 = n_o^2$, and $\epsilon_{zr} = \epsilon_z/\epsilon_0 = n_e^2$. The dielectric loss of the permittivity is neglected in the study. The time harmonic waves that propagate in the z -direction can be expressed as:

$$\exp[i(k_x x + k_z z - \omega t)] \quad (2)$$

where k_i represents the i component of wave vector in the i direction, $k_y = 0$ has been assumed for homogeneity in the y -direction, and ω is angular frequency. Since the system shows the mirror symmetry $\mathcal{M}_y: (x, y, z) \rightarrow (x, -y, z)$, the guided wave is cataloged into two polarization modes, TE with non-zero electric field perpendicular to the mirror plane (any xz plane due to uniformity in the y -direction) and TM with non-zero electric field parallel to the mirror plane (any xz plane due to uniformity in the y -direction) [Ref. 34]. By expressing the field components and

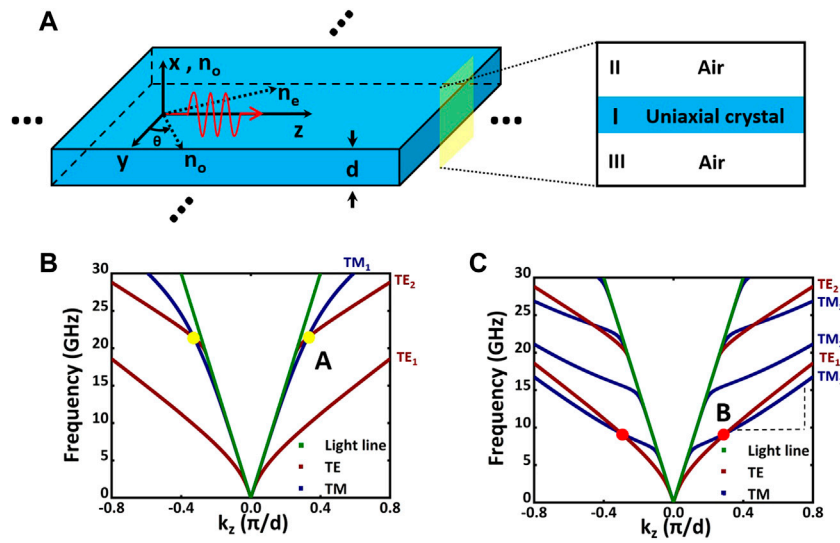


FIGURE 2

(A) The schematic picture of the anisotropic dielectric slab waveguide, where (x, y, z) is the coordinate system for the slab; (n_o, n_o, n_e) is the dielectric principal axes for the anisotropic permittivity. The red arrow represents the propagation direction of electromagnetic wave. The panel in the right shows the three layers structure in our system. The slab thickness $d = 2$ mm. (B) Dispersion diagram of TE and TM modes in the negatively uniaxial case when $\epsilon_z = 4\epsilon_0$. The degenerate points are marked with yellow dots. (C) Dispersion diagram of TE and TM modes in the positively uniaxial case when $\epsilon_z = 100\epsilon_0$. The degenerate points that we will investigate in details are marked with red dots. The velocity or effective index of the first-order modes (TM_1 and TE_1) near the point B is approximated by the slope estimation $\Delta\omega/\Delta k_z$, as depicted by the right-angled dash lines.

matching the boundary conditions on the two surfaces of the slab, we can get the characteristic equations for TE mode:

$$2\alpha k_x \cos k_x d + (\alpha^2 - k_x^2) \sin k_x d = 0 \tag{3}$$

$$k_x^2 + k_z^2 = \epsilon_{yr} k_0^2 \tag{4}$$

and for TM mode:

$$\left(\alpha^2 - \frac{k_x^2}{\epsilon_{zr}}\right) \sin k_x d + \frac{2\alpha k_x}{\epsilon_{zr}} \cos k_x d = 0 \tag{5}$$

$$\frac{k_x^2}{\epsilon_{zr}} + \frac{k_z^2}{\epsilon_{xr}} = k_0^2 \tag{6}$$

Above, Eqs 4, 6 are the dispersion relation in regime I, α is the imaginary part of perpendicular component of wave vector in theregime II and III, and $k_0 = \omega/c$ with the speed of light in vacuum $c = 1/\sqrt{\epsilon_0\mu_0}$, which satisfies:

$$k_z^2 - \alpha^2 = k_0^2 \tag{7}$$

For concreteness, we choose $\epsilon_x = \epsilon_y = 16\epsilon_0$, and switch the value of ϵ_z for negatively uniaxial case ($\epsilon_z = 4\epsilon_0$) and positively uniaxial case ($\epsilon_z = 100\epsilon_0$). It is has known that 2D dielectric slabs have been extensively used as basic waveguides in microwave engineering and devices where a broad horizon of dielectric materials, e.g., high- k printed circuit board (PCB) and ceramics, may offer various permittivity including such values [36, 37]. The calculated results are shown in Figures 2B,C. Within a qualitative physical picture, we approximate the slope of TM

modes beyond the light line to be roughly $\sim c/n_{eff}^{TM}$, and the effective index $n_{eff}^{TM} = \sqrt{\epsilon_{eff}^{TM}/\epsilon_0} \approx \sqrt{avg(\epsilon_x, \epsilon_z)/\epsilon_0}$, where the effective permittivity ϵ_{eff}^{TM} for TM mode can be regarded to some degree as special average of $\epsilon_x; \epsilon_z$ because the electric field is oriented along both x - and z -direction. In contrast, the slope, being roughly $\sim c/n_{eff}^{TE}$, of TE modes is related to $n_{eff}^{TE} = \sqrt{\epsilon_{eff}^{TE}/\epsilon_0} \approx \sqrt{\epsilon_y/\epsilon_0}$ in terms of the y -orientation of electric field. Therefore, given $\epsilon_x = \epsilon_y$ and when switching only ϵ_z from the negatively uniaxial case ($\epsilon_z < \epsilon_y$) to positively uniaxial case ($\epsilon_z > \epsilon_y$), we see that the slopes of the TE modes remain almost unchanged whereas the TM ones change expectedly in the dispersion diagram, as comparing Figure 2B with Figure 2C.

It is noted that the first-order TM mode (TM_1) crosses with the second-order TE mode (TE_2) for the negatively uniaxial case ($\epsilon_z = 4\epsilon_0$), as labeled by point A in Figure 2B, and that it crosses with the first-order TE mode for positively uniaxial case ($\epsilon_z = 100\epsilon_0$), as labeled by point B in Figure 2C, where TM curves are generally less steep than TE ones. For instance, the slope of TM_1 near the point B is estimated as $\frac{\Delta\omega}{\Delta k_z} \sim \frac{2\pi*7.48GHz}{0.5\pi/d} \sim c/5$ that corresponds to $\epsilon_{eff}^{TM1}/\epsilon_0 \sim 25$, whereas the slope of TE_1 near the point B is estimated as $\frac{\Delta\omega}{\Delta k_z} \sim \frac{2\pi*9.34GHz}{0.5\pi/d} \sim c/4$ that corresponds to $\epsilon_{eff}^{TE1}/\epsilon_0 \sim 16$. Therefore, the decrease in the slope of TM modes with ϵ_z leads to the switch of one of degenerating bands from TE_2 (point A) to TE_1 (point B). In addition, as increasing ϵ_z , more

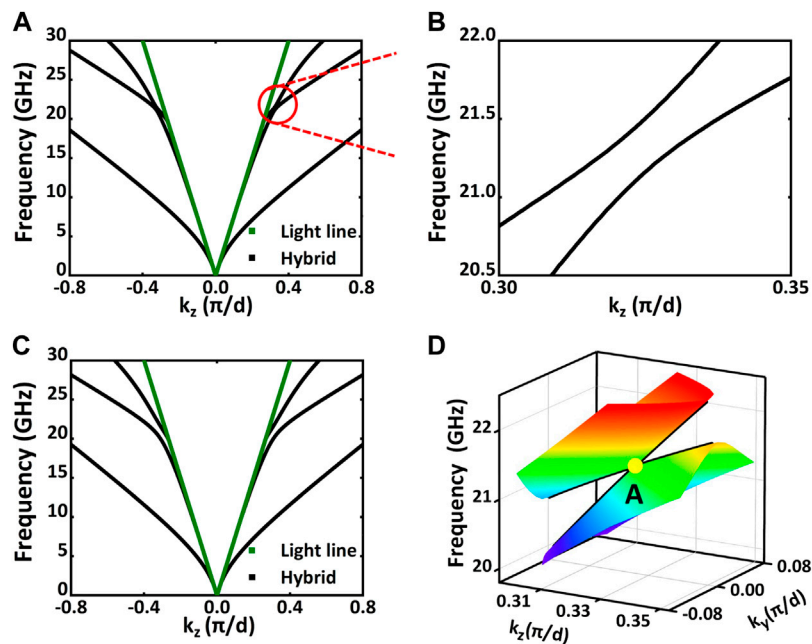


FIGURE 3

Type-II Dirac point in the dispersion diagram of the negatively uniaxial crystal slab when $\varepsilon_z = 4\varepsilon_0$. (A) Shows the dispersion relation when θ is chosen as 2° . (B) Zoom-in view of the band gap in (A). (C) Shows the dispersion relation when $\theta = 10^\circ$. (D) 3D view around the degeneracy that gives rise to a type-II Dirac point in momentum space.

TM modes appear in Figure 2C, and TM_3 is crossing with TE_2 , which gives rise to more degeneracies at higher frequencies (see Section A in Supplementary Materials).

Type-II Dirac degeneracy in uniaxial crystal slabs

In order to exhibit the complete dispersion structure around the degenerate points, we need calculate the band diagram $\omega(k_y, k_z)$. In the calculation, we first rotate the in-plane dielectric principal axes around the x -direction with the angle θ , as shown in Figure 2A. The non-diagonalized permittivity tensor ε_θ after rotation can be written as

$$\bar{\varepsilon}_\theta = \begin{bmatrix} \varepsilon_{xx} & 0 & 0 \\ 0 & \varepsilon_{yy} & \varepsilon_{yz} \\ 0 & \varepsilon_{zy} & \varepsilon_{zz} \end{bmatrix} \quad (8)$$

in which

$$\varepsilon_{xx} = \varepsilon_x \quad (9)$$

$$\varepsilon_{yy} = \varepsilon_y \cos^2 \theta + \varepsilon_z \sin^2 \theta \quad (10)$$

$$\varepsilon_{zz} = \varepsilon_z \cos^2 \theta + \varepsilon_y \sin^2 \theta \quad (11)$$

$$\varepsilon_{yz} = \varepsilon_{zy} = (\varepsilon_y - \varepsilon_z) \sin \theta \cdot \cos \theta \quad (12)$$

Then, we assume that the waves still propagate along the z -direction and express the electric fields and magnetic fields in

different regions. Because the mirror symmetry \mathcal{M}_y is broken under the rotation, the guided modes are no longer pure TE or TM mode, but are their combination which we call hybrid mode. The characteristic equation for hybrid modes is solved by matching boundary conditions, which gives us the dispersion $\omega_\theta(k_z)$. Finally, the dispersion $\omega(k_y, k_z)$ is obtained through a standard map from polar coordinate to Cartesian coordinate. Although the calculation is based on the rotated dielectric principal axis, the results are the same as those of rotating the (x, y, z) coordinate system while maintaining the dielectric principal axis, because both are the equivalent description of rotation.

We first analyze the degenerate point A in negatively uniaxial case with $\varepsilon_z = 4\varepsilon_0$, where it is the lowest degeneracy in frequency, as displayed in Figure 2B. We calculate the dispersion $\omega_\theta(k_z)$ when varying the angle θ , and the degeneracy is seen to become gapped upon θ being nonzero, as shown in Figures 3A–C. Combining all θ -cut plots, we can achieve the three-dimensional (3D) view of band diagram $\omega(k_y, k_z)$ in momentum space, as depicted in Figure 3D. The band structure around A exhibits the characteristic of two over-tilted cones, and thus the degeneracy is just the type-II DP. The gapping reason is that the two modes display the like parity in the mirror symmetry $\mathcal{M}_x: (x, y, z) \rightarrow (-x, y, z)$ (the symmetry classifies all modes as even or odd parity with respect to the mirror plane $x = 0$, see Section B in Supplementary Materials) and simultaneously \mathcal{M}_y is broken upon $\theta \neq 0$. Such 2D type-II DP has been observed in the artificially designed metasurfaces with

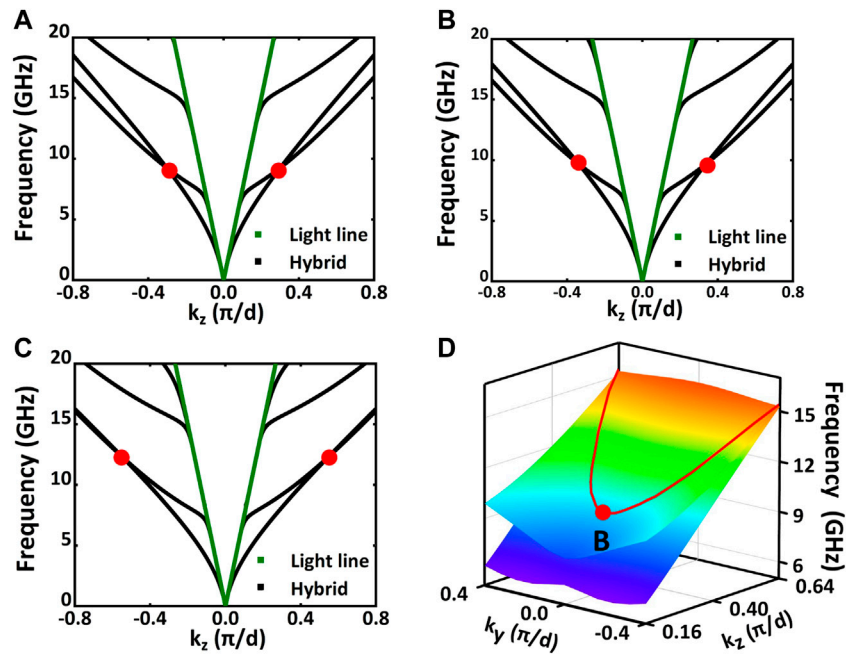


FIGURE 4 Type-II Dirac line in the dispersion diagram of the positively uniaxial crystal slab when $\epsilon_z = 100\epsilon_0$. shows the dispersion relation when θ is chosen as 2° , 15° and 30° , where the red points label the linear cross of bands. 3D view around the (A-C) degeneracy B (red point), where all degenerated points give rise to the Type-II Dirac line in momentum space, which is (D) marked by red line.

periodic metallic patterns at microwave frequencies [38–40]. In contrast, our system is of no discrete translational symmetry, but continuous in space.

Next, let’s focus our attention on the degenerate point *B* in positively uniaxial case with $\epsilon_z = 100\epsilon_0$. Interestingly, in the cut plot with different θ , the degeneracy persists, which forms a section of line in momentum space, as plotted in Figure 4. According to the slope of two crossing bands, such degeneracy is the Type-II DL. The degeneracy is protected by the mirror symmetry \mathcal{M}_x , in which the two bands display the opposite parity (see Section B in Supplementary Materials), and would be gapped if the uniaxial crystal slab lies in an asymmetric background, (see Section C in Supplementary Materials).

It is also noted from Figure 4C that the two bands, responsible for the Dirac line, almost coincide with each other when θ comes to 30° . If we increase the rotation angle further, the DL degeneracy will lift. The physical reason can be understood qualitatively from an effective permittivity point of view. Although being hybrid in nature upon $\theta \neq 0$, the two bands are dominated, respectively, by the TE_1 and TM_1 modes and can be considered as their descendants. As increasing the angle θ , the slope of TE-like dispersion curve will decrease from $\sim c/\sqrt{\epsilon_y/\epsilon_0}$ at $\theta = 0$ to $\sim c/\sqrt{\epsilon_{eff}^{TE-like}(\epsilon_y, \epsilon_z, \theta)/\epsilon_0}$ at $\theta \neq 0$ where the effective permittivity $\epsilon_{eff}^{TE-like}$ is the θ -mediated average between ϵ_y and ϵ_z , and we make the approximation $\epsilon_{eff}^{TE-like}(\epsilon_y, \epsilon_z, \theta)/\epsilon_0 \approx n_{eff}^2(\theta) = n_o^2 n_e^2 / (n_o^2 \sin^2 \theta + n_e^2 \cos^2 \theta)$ (the relation expressed for extraordinary light in the bulk crystal [Ref. 35]). Consequently, the

slope of TE-like dispersion may become comparable to that of TM-like dispersion upon some angle, and appear less than the latter beyond the angle, and such slope difference does not lead to the degeneracy any more. The threshold angle θ_c can be estimated through requiring the slope equality $\epsilon_{eff}^{TE-like}(\epsilon_y, \epsilon_z, \theta_c) = \epsilon_{eff}^{TM-like}(\epsilon_x, \epsilon_z)$, where we assume $\epsilon_{eff}^{TM-like}(\epsilon_x, \epsilon_z) \approx \epsilon_{eff}^{TM1} \sim 25\epsilon_0$ after noticing insignificant θ -dependence of TM-like dispersions in Figure 4. Thus, the threshold angles are solved as $\theta_{c1} \sim \pm 40^\circ$ and $\theta_{c2} \sim \pm 140^\circ$, which are quite close to the numerical values $\pm 35^\circ$ and $\pm 145^\circ$ from COMSOL simulation and correspond to the $+k_z$ and $-k_z$ directions, respectively. Overall, this kind of nodal line is essentially different from the loop degeneracy [Ref. 40] because it cannot construct a closed loop in momentum space.

Discussions

When investigating the propagation of the guided modes along the direction perpendicular to the optical axis (e.g., the propagation along y -axis while the optical axis being z -axis, and the mirror symmetry $\mathcal{M}_z: (x, y, z) \rightarrow (x, y, -z)$ giving rise to the TE/TM modes), we find that the relative magnitude between the slopes of TM and TE modes will swap, because TE waves have the electric field polarized along the optical axis ϵ_z or n_e and TM waves have the electric field components along both x - and y -directions. Thus, the DL degeneracy from the lowest two modes (even and odd parity)

will occur to the negatively uniaxial case, and the DP degeneracy from the higher-order modes will appear in the positively uniaxial case (see Section D in Supplementary Materials).

In addition, we present a microwave metamaterial design which approximates at lower frequencies a positively uniaxial crystal with dispersive permittivity component, and the band degeneracy shows the similarity to and the difference from the case of the continuous crystal slab (see Section E in Supplementary Materials).

Conclusion

In conclusion, by controlling positivity/negativity of the refractive index ellipsoid, we can obtain the nodal point and nodal line degeneracies for the guided modes on the uniaxial crystal slab waveguide. Furthermore, the point and line characteristics and their connections with the refractive index ellipsoid can be swapped through switching the propagation direction. Our results link the band degeneracy with positivity/negativity of the uniaxial crystal, and provide a new approach to regulate the topology of degeneracy in 2D photonic bands.

Data availability statement

The original contributions presented in the study are included in the article/supplementary material, further inquiries can be directed to the corresponding author.

Author contributions

BH conceived and supervised the research; XP performed the research; HL, WD, XZ, KX, CH, and GW assisted in analyzing the data; and BH, XP, and HL wrote the manuscript.

References

1. Armitage NP, Mele EJ, Vishwanath A. Weyl and Dirac semimetals in three-dimensional solids. *Rev Mod Phys* (2018) 90:015001. doi:10.1103/revmodphys.90.015001
2. Li S, Yu Z-M, Yao Y, Yang SA. Type-II topological metals. *Front Phys* (2020) 15(4):43201. doi:10.1007/s11467-020-0963-7
3. Lu L, Joannopoulos JD, Soljačić M. Topological photonics. *Nat Photon* (2014) 8:821–9. doi:10.1038/nphoton.2014.248
4. Kim M, Jacob Z, Rho J. Recent advances in 2D, 3D and higher-order topological photonics. *Light Sci Appl* (2020) 9:130. doi:10.1038/s41377-020-0331-y
5. Park HD, Gao W, Zhang X, Oh SS. Nodal lines in momentum space: Topological invariants and recent realizations in photonic and other systems. *Nanophotonics* (2022) 11(11):2779–801. doi:10.1515/nanoph-2021-0692
6. Lu L, Wang Z-Y, Ye D-X, Ran L-X, Fu L, Joannopoulos JD, et al. Experimental observation of Weyl points. *Science* (2015) 349:622–4. doi:10.1126/science.aaa9273
7. Gao W, Yang B, Lawrence M, Fang F, Béril B, Zhang S. Photonic Weyl degeneracies in magnetized plasma. *Nat Commun* (2016) 7:12435. doi:10.1038/ncomms12435
8. Yang B, Guo Q, Tremain B, Barr LE, Gao W, Liu H, et al. Direct observation of topological surface-state arcs in photonic metamaterials. *Nat Commun* (2017) 8:97. doi:10.1038/s41467-017-00134-1

Funding

This work was supported by the Natural Science Foundation of China (NSFC) (Grant No. 12074279), the Major Program of Natural Science Research of Jiangsu Higher Education Institutions (Grant No.18KJA140003), and the Priority Academic Program Development (PAPD) of Jiangsu Higher Education Institutions.

Conflict of interest

Chuangeng Hu was employed by Shenzhen Fantwave Tech Co., Ltd

The remaining authors declare that the research was conducted in the absence of any commercial or financial relationships that could be construed as a potential conflict of interest.

Publisher's note

All claims expressed in this article are solely those of the authors and do not necessarily represent those of their affiliated organizations, or those of the publisher, the editors and the reviewers. Any product that may be evaluated in this article, or claim that may be made by its manufacturer, is not guaranteed or endorsed by the publisher.

Supplementary material

The Supplementary Material for this article can be found online at: <https://www.frontiersin.org/articles/10.3389/fphy.2022.1095669/full#supplementary-material>

9. Yang B, Guo Q, Tremain B, Liu R, Barr LE, Yan Q, et al. Ideal Weyl points and helioid surface states in artificial photonic crystal structures. *Science* (2018) 359:1013–6. doi:10.1126/science.aaq1221
10. Qiu P, Qiu W, Lin Z, Chen H, Ren J, Wang J-X, et al. Double Dirac point in a photonic graphene. *J Phys D: Appl Phys* (2017) 50:335101. doi:10.1088/1361-6463/aa7bc2
11. Xiao M, Lin Q, Fan S. Hyperbolic Weyl point in reciprocal chiral metamaterials. *Phys Rev Lett* (2016) 117:057401. doi:10.1103/physrevlett.117.057401
12. Yang Y, Gao Z, Feng X, Huang Y-X, Zhou P, Yang SA, et al. Ideal unconventional Weyl point in a chiral photonic metamaterial. *Phys Rev Lett* (2020) 125:143001. doi:10.1103/physrevlett.125.143001
13. Liu G-G, Zhou P, Yang Y, Xue H, Ren X, Lin X, et al. Observation of an unpaired photonic Dirac point. *Nat Commun* (2020) 11:1873. doi:10.1038/s41467-020-15801-z
14. Luo L, Deng W, Yang Y, Yan M, Lu J, Huang X, et al. Observation of quadruple Weyl point in hybrid-Weyl phononic crystals. *Phys Rev B* (2022) 106:134108. doi:10.1103/physrevb.106.134108
15. Huang X, Lai Y, Hang ZH, Zheng H, Chan CT. Dirac cones induced by accidental degeneracy in photonic crystals and zero-refractive-index materials. *Nat Mater* (2011) 10:582–6. doi:10.1038/nmat3030

16. Xu C, Ma G, Chen Z-G, Luo J, Shi J, Lai Y, et al. Three-dimensional acoustic double-zero-index medium with a fourfold degenerate Dirac-like point. *Phys Rev Lett* (2020) 124:074501. doi:10.1103/physrevlett.124.074501
17. Lin JY, Hu NC, Chen YJ, Lee CH, Zhang X. Line nodes, Dirac points, and Lifshitz transition in two-dimensional nonsymmorphic photonic crystals. *Phys Rev B* (2017) 96:075438. doi:10.1103/physrevb.96.075438
18. Yang S-Y, Yang H, Derunova E, Parkin SSP, Yan B, Ali MN. Symmetry demanded topological nodal-line materials. *Adv Phys* (2018) 3:1414631. doi:10.1080/23746149.2017.1414631
19. Feng B, Fu B, Kasamatsu S, Ito S, Cheng P, Liu C-C, et al. Experimental realization of two-dimensional Dirac nodal line fermions in monolayer Cu₂Si. *Nat Commun* (2017) 8:1007. doi:10.1038/s41467-017-01108-z
20. Feng B, Zhang R-W, Feng Y, Fu B, Wu S, Miyamoto K, et al. Discovery of Weyl nodal lines in a single-layer ferromagnet. *Phys Rev Lett* (2019) 123:116401. doi:10.1103/physrevlett.123.116401
21. Wang S-S, Yu Z-M, Liu Y, Jiao Y, Guan S, Sheng X-L, et al. Two-dimensional nodal-loop half-metal in monolayer MnN. *Phys Rev M* (2019) 3:084201. doi:10.1103/physrevmaterials.3.084201
22. You J-Y, Chen C, Zhang Z, Sheng X-L, Yang SA, Su G. Two-dimensional Weyl half-semimetal and tunable quantum anomalous Hall effect. *Phys Rev B* (2019) 100:064408. doi:10.1103/physrevb.100.064408
23. Gao W, Yang B, Tremain B, Liu H, Guo Q, Xia L, et al. Experimental observation of photonic nodal line degeneracies in metacrystals. *Nat Commun* (2018) 9:950. doi:10.1038/s41467-018-03407-5
24. Qiu H, Qiu C, Yu R, Xiao M, He H, Ye L, et al. Straight nodal lines and waterslide surface states observed in acoustic metacrystals. *Phys Rev B* (2019) 100:041303. doi:10.1103/physrevb.100.041303
25. Deng W, Lu J, Li F, Huang X, Yan M, Ma J, et al. Nodal rings and drumhead surface states in phononic crystals. *Nat Commun* (2019) 10:1769. doi:10.1038/s41467-019-09820-8
26. Xiong Z, Zhang R-Y, Yu R, Chan CT, Chen Y. Hidden symmetry enforced nexus points of nodal lines in layer-stacked dielectric photonic crystals. *Light Sci Appl* (2020) 9:176. doi:10.1038/s41377-020-00382-9
27. Hu M, Zhang Y, Jiang X, Qiao T, Wang Q, Zhu S, et al. Double-bowl state in photonic Dirac nodal line semimetal. *Light Sci Appl* (2021) 10:170. doi:10.1038/s41377-021-00614-6
28. Deng W-M, Chen Z-M, Li M-Y, Guo C-H, Tian Z-T, Sun K-X, et al. Ideal nodal rings of one-dimensional photonic crystals in the visible region. *Light Sci Appl* (2022) 11:134. doi:10.1038/s41377-022-00821-9
29. Yan Q, Liu R, Yan Z, Liu B, Chen H, Wang Z, et al. Experimental discovery of nodal chains. *Nat Phys* (2018) 14(5):461–4. doi:10.1038/s41567-017-0041-4
30. Wang Y, Zhou X, Li S, Zhang W, Hu C, Lu W, et al. Flatness and boundness of photonic drumhead surface state in a metallic lattice. *Sci Rep* (2021) 11:8684. doi:10.1038/s41598-021-88004-1
31. Wu X, Fan H, Liu T, Gu Z, Zhang R-Y, Zhu J, et al. Topological phononics arising from fluid-solid interactions. *Nat Commun* (2022) 13:6120. doi:10.1038/s41467-022-33896-4
32. Xiao M, Ye L, Qiu C, He H, Liu Z, Fan S. Experimental demonstration of acoustic semimetal with topologically charged nodal surface. *Sci. Adv.* (2020) 6:eav2360.
33. Yang Y, Xia J-P, Sun H-X, Ge Y, Jia D, Yuan S-Q, et al. Observation of a topological nodal surface and its surface-state arcs in an artificial acoustic crystal. *Nat Commun* (2019) 10:5185. doi:10.1038/s41467-019-13258-3
34. Joannopoulos JD, Meade RD, Johnson SG, Joshua N. *Photonic crystals: Molding the flow of light*. 2nd ed. Princeton, NJ: Princeton University Press (2011).
35. Saleh BEA, Teich MC. *Fundamentals of photonics*. 2nd ed. New York, NY: John Wiley & Sons (2007).
36. Pozer DM, Appendix G. *Microwave engineering*. 2nd ed. New York, NY: John Wiley & Sons (1998).
37. ROGERSPCB MAIN (2020). Rogers laminates in stock. Available at: <https://www.rogerspcb.com.cn/>.
38. Hu C, Li Z, Tong R, Wu X, Xia Z, Wang L, et al. Type-II Dirac photons at metasurfaces. *Phys Rev Lett* (2018) 121:024301. doi:10.1103/physrevlett.121.024301
39. Li H, Hu C, Zhou X, Lu W, Hou B, Wen W. Conical diffraction from type-II Dirac point at metasurfaces. *EPL* (2020) 130:17007. doi:10.1209/0295-5075/130/17007
40. Li H, Hu C, Jiang J-H, Wu J, Wen W, Hou B. Photonic type-III nodal loop and topological phase transitions at bilayer metasurfaces. *Front Mater* (2022) 9:909381. doi:10.3389/fmats.2022.909381